

High-Performance Mid-IR to Deep-UV van der Waals Photodetectors Capable of Local Spectroscopy at Room Temperature

Daozhi Shen^{1,2,3}, HeeBong Yang^{1,4,#}, Christian Spudat^{1,4,5,#}, Tarun Patel^{1,6}, Shazhou Zhong^{1,6}, Fangchu Chen^{1,6}, Jian Yan^{7,8}, Xuan Luo⁷, Meixin Cheng^{2,9}, Germán Sciaini^{2,9}, Yuping Sun^{7,10,11}, Daniel A. Rhodes¹², Thomas Timusk¹³, Y. Norman Zhou^{3,9}, Na Young Kim^{1,4,9}, and Adam W. Tsen^{1,2,9,*}

¹ Institute for Quantum Computing, University of Waterloo, Waterloo, ON, Canada N2L 3G1

² Department of Chemistry, University of Waterloo, Waterloo, ON, Canada N2L 3G1

³ Centre for Advanced Materials Joining and Department of Mechanical and Mechatronics Engineering, University of Waterloo, Waterloo, Ontario, Canada N2L 3G1

⁴ Department of Electrical and Computer Engineering, University of Waterloo, Waterloo, ON, Canada N2L 3G1

⁵ Institute of Electrodynamics, Microwave and Circuit Engineering, TU Wien, Gusshausstrasse 25/354, 1040 Vienna, Austria

⁶ Department of Physics and Astronomy, University of Waterloo, Waterloo, ON, Canada N2L 3G1

⁷ Key Laboratory of Materials Physics, Institute of Solid State Physics, HFIPS, Chinese Academy of Sciences, Hefei, China 230031

⁸ University of Science and Technology of China, Hefei, China 230026

⁹ Waterloo Institute for Nanotechnology, University of Waterloo, Waterloo, Ontario, Canada N2L 3G1

¹⁰ Anhui Province Key Laboratory of Condensed Matter Physics at Extreme Conditions, High Magnetic Field Laboratory, HFIPS, Chinese Academy of Sciences, Hefei, China 230031

¹¹ Collaborative Innovation Center of Advanced Microstructures, Nanjing University, Nanjing, China 210093

¹² Department of Materials Science and Engineering, University of Wisconsin-Madison, WI, USA

¹³ Department of Physics and Astronomy, McMaster University, Hamilton, Ontario, Canada L8S 4M1

#These authors contribute equally.

*Corresponding author: awtsen@uwaterloo.ca

The ability to perform broadband optical spectroscopy with sub-diffraction-limit resolution is highly sought-after for a wide range of critical applications from nanophotonics and spectral imaging to materials and quantum information science. However, sophisticated tip-enhanced techniques combined with broadband synchrotron or multiple laser sources and cryogenically cooled detectors are currently required to achieve this goal, thus limiting their widespread applicability. We bypass this challenge by demonstrating an extremely broadband photodetector based on a two-dimensional (2D) van der Waals heterostructure that is sensitive to light across over a decade in energy from the mid-infrared (MIR) to deep-ultraviolet (DUV) at room temperature. The devices feature high detectivity ($> 10^9 \text{ cm Hz}^{1/2} \text{ W}^{-1}$) together with ultra-fast response speed ($< 200 \text{ ns}$) that is not achievable by existing broadband detectors. The active area can be further miniaturized to submicron dimensions, far below the diffraction limit for the longest detectable wavelength of $4.1 \mu\text{m}$, enabling such devices for facile measurements of local optical properties on atomic-layer-thickness samples placed in close proximity. This work can lead to the development of low-cost and high-throughput photosensors for hyperspectral imaging at the nanoscale.

Broadband optical spectroscopies, such as reflectance and absorption, from the infrared (IR) to ultraviolet (UV) are a powerful, noninvasive probe commonly used to characterize the structural, chemical, and electronic properties of all material systems¹. Optical measurements are generally limited by diffraction, however, which imposes a tradeoff between the smallest detectable photon energy and probe area that is given by the relation: illumination spot size $\gtrsim \lambda/2$, at a given wavelength λ in air. This makes local spectroscopy in the longer wavelength IR regime especially difficult and imposes stringent restrictions on material uniformity that is often unachievable. One solution to this challenge is to exploit tip-enhanced

near-field techniques²; although, they collectively carry disadvantages of high cost and low throughput, while simultaneously requiring the use of a broadband source with sufficient intensity^{3,4}. Alternatively, it may be possible to obtain local spectroscopic information on nonuniform systems with conventional widefield illumination by instead placing the area of interest in proximal contact to an ultrasmall photodetector. This conceptual photodetection scheme is illustrated in Figure 1a. Wavelength-dependent photocurrent measurements taken with and without the sample can then be compared to determine the local absorbance spectrum, as shown in Figure 1b. Here, the photocurrent ($I_{pc} = I_{light} - I_{dark}$) is defined as difference in device current with light (I_{light}) and without (I_{dark}).

While the latter detection scheme can be more easily implemented compared to tip-enhanced illumination, it also places stricter requirements on the capabilities of the detector: broadband response, high sensitivity, fast response speed, and miniaturizability are needed, ideally together with room temperature operability. To the best of our knowledge, such high-performance broadband detectors have not yet been demonstrated. Although thermopile sensors and some phototransistors based on 2D materials have high sensitivity and wide detection range⁵⁻⁸, their response speed (several to hundreds of milliseconds) is too slow to yield spectroscopic data with reasonable throughput. Miniaturized broadband detectors present additional difficulties. Even though silicon-based sensors can be readily scaled to the micron size, they are transparent to photon energies below ~ 1.1 eV. Similarly, local photodetectors based on various nanostructures have only demonstrated a responsivity in the visible range^{9,10}.

To address these challenges, we first report a vertical photodetector device concept based on 2D materials with multiple bandgaps that is sensitive to radiation across a decade in energy from the mid-IR (MIR) to deep-UV (DUV), or 0.3 to 5.0 eV, at room temperature. The photocurrent spectrum is further tunable with bias voltage and can be optimized to reach a peak specific detectivity of 3.4×10^9 cm Hz^{1/2} W⁻¹ in the MIR. The device response time is < 200 ns, the fastest yet reported for detectors with DUV to MIR sensitivity^{5-7,11-13}. To understand the overall device behavior, we build a numerical finite element analysis model of the entire heterostructure and identify the bias-voltage-dependent band diagrams and carrier concentrations. Then, we show using scanning photocurrent measurements that the active area can be made far smaller than the diffraction limit for the lowest energy of detectable IR radiation, enabling such devices for direct measurements of local optical properties. We demonstrate this latter capability experimentally by performing broadband absorption spectroscopy of different 2D materials down to the monolayer limit using conventional wide-field illumination.

Figure 1a also shows a schematic of our device geometry and measurement circuit. Few-layer graphene (Gr) provides a transparent top electrode and semiconducting 2H-MoTe₂ is used as a middle layer to absorb light above 0.9 eV energy. Small-bandgap black phosphorus (BP) serves both as a bottom conductor and absorber for light energy down to 0.3 eV. The heterostructures are assembled by dry-transfer within a nitrogen-filled glovebox and covered by a thin insulating layer of hexagonal boron nitride (hBN), which is transparent to light below 5.9 eV, to protect the BP from degradation in the ambient measurement environment (see Method for details of crystal synthesis and device fabrication). Absorbance spectra of the two semiconductors are plotted in the upper panel of Figure 2a. While BP has been previously demonstrated to be an excellent photodetector in the IR range¹⁴⁻¹⁶, we find this particular combination of materials and device geometry allows for a continuous spectral response from the MIR to the DUV with exceptional performance. Substituting MoTe₂ with a larger bandgap semiconductor may leave a gap in the response spectrum. Although any MoTe₂ and BP flake thickness larger than ~ 2 nm and ~ 10 nm, respectively, will yield a bandgap close to that of the bulk crystal^{17,18}, we determined that specifically ~ 10 -nm-thick MoTe₂ and ~ 17 -nm-thick BP will produce higher responsivity (see Figure S1).

The middle panel of Figure 2a shows the photocurrent spectral response of a typical device with relatively large junction area ($15 \mu\text{m} \times 18 \mu\text{m}$) at several different voltage biases. The full bias dependence of the spectrum is provided in Figure S2. At zero bias, the overall photoresponse is relatively weak. Upon increasing positive voltage between BP and Gr, the response in the near-IR (NIR) and visible is

continuously increased, but no response is observed below 0.95 eV. The two peaks at 1.06 eV and 1.72 eV correspond to the A and A' excitons in MoTe₂, as can be seen in the absorption spectrum¹⁸. Upon increasing negative voltage, the response from MoTe₂ is similarly increased; however, the response from BP at lower energies increases as well. In particular, the MoTe₂ A exciton peak picks up where the BP response decays. The net result is a continuous spectral response from the MIR at 0.3 eV to the visible when a small negative voltage is applied to our photodetector, a key finding of this work. The decay at high energies is attributed to the low intensity of the tungsten source. As we shall show, the detector exhibits significant responsivity up to 5.0 eV, the highest energy measured, yielding a spectral range of over a full decade. For comparison, the bottom panel of Figure 2a presents the spectral response of three widely used commercial photodetectors based on Si, InGaAs and mercury cadmium telluride (MCT), respectively, measured using the same setup (see Methods for details). Clearly, a combination of these detectors is needed to cover the same spectral range as our devices.

We now proceed to characterize the transport properties of our photodetectors in detail. Without illumination, the I - V characteristics of the $15\ \mu\text{m} \times 18\ \mu\text{m}$ device exhibit diode-like rectifying behavior, as shown in Figure 2b. Using finite element numerical simulations of the heterostructure (see Methods), we can achieve close fitting between the calculated and experimentally observed dark transport characteristics (Figure S3). A series of band alignments and carrier concentration profiles for various bias conditions are then extracted and given in Figures S4 and 5, respectively. At zero and forward bias ($V \geq 0$), the BP/MoTe₂ interface forms a hole-accumulation region owing to the intrinsically p-doped BP¹⁹. These holes are the dominant carrier concentration of the entire heterostructure, and so contribute to relatively large current levels for $V > 0$ after surmounting the MoTe₂ barrier. Under reverse bias ($V \lesssim -0.3\text{V}$), however, a comparably smaller population of electrons accumulate at the same interface, leading to relatively less current. This asymmetry can be directly observed in the representative band diagrams shown in Figure 2c for $V = \pm 0.5\ \text{V}$, and is further schematized by the dark carriers and arrows in gray.

Figure 2b also shows the I - V characteristics of the same device under illumination by focused lasers of several different wavelengths with the same power and polarization. When we use a visible ($\lambda = 520\ \text{nm}$) or NIR ($\lambda = 820\ \text{nm}$) laser, whose energy is larger than the MoTe₂ bandgap energy, we observe a large increase in device current with light, or photocurrent I_{pc} , for both bias directions. As photocarriers are predominantly generated in the upper MoTe₂ layer for this photon energy regime, both forward and reverse bias lead to barrierless transport and relatively efficient collection of these carriers, and so $I_{pc} > I_{dark}$ for nearly all V . This effect is captured by the blue carriers and arrows in Figure 2c.

When we use IR lasers ($\lambda = 1310, 2400\ \text{nm}$), on the other hand, large photocurrent flows only under reverse bias, and not forward bias, which is consistent with the bias dependence of the full photocurrent spectrum (Figure 2a). In general, we expect the photocurrent to be suppressed if the number of dark carriers greatly exceed that of the photo-generated carriers. As the interfacial carrier concentration under forward bias is significantly greater than that under reverse bias (see Figure S5), $I_{pc} \ll I_{dark}$ for $V \geq 0$ when the photon energy is below the MoTe₂ bandgap. This bias asymmetry is illustrated by the red carriers and arrows in Figure 2c. In short, to obtain the broadest spectral photoresponse, BP must be negatively biased against Gr in our device geometry, and so we primarily focus on this regime for the remainder of this work.

We next set out to determine the optimal light excitation and bias conditions at which to evaluate the various performance metrics of our $15\ \mu\text{m} \times 18\ \mu\text{m}$ photodetector (responsivity, quantum efficiency, detectivity, and response speed). First, in Figure 3a, we show the laser power dependence of I_{pc} for various incident wavelengths. The response is linear below $\sim 5\ \mu\text{W}$ for all wavelengths, but gradually saturates with increasing power, and so we shall stay within the linear regime for subsequent measurements.

Figure 3b displays normalized I_{pc} as a function of the linear polarization angle of the laser for three wavelengths. For $\lambda = 2300\ \text{nm}$ (0.52 eV), light absorption is almost solely attributed to BP, which is known to be stronger (weaker) for polarization along the armchair (zigzag) direction^{14,20,21}. We thus identify the

maximal I_{pc} lobes as the BP armchair angle. For $\lambda = 520$ nm (2.4 eV), I_{pc} is almost fully symmetric, which indicates that the photocarriers are mainly generated by light absorption from MoTe₂. For $\lambda = 1310$ nm (0.95 eV), we observe an intermediate level of asymmetry.

For the polarization angle yielding maximum I_{pc} , we show in Figure 3c the device responsivity (\mathfrak{R}) as a function of laser energy up to 3.1 eV and bias voltage in a continuous 2D false-color plot. We have boxed the regions where BP or MoTe₂ primarily contribute to the photoresponse. Photocurrent at high energies is mainly due to MoTe₂ absorption at all biases, with an optimum \mathfrak{R} of ~ 0.15 A/W at 1.88 eV and -0.23 V. The low energy response at negative bias is due to BP and exhibits \mathfrak{R} as high as ~ 0.2 A/W at 0.54 eV and -0.3 V. There is also an inaccessible region (hashed area in Figure 3c) at positive bias and low energy. While the spectral response is highly tunable with voltage, it appears a single negative bias near -0.3 V (marked by the red arrow) can be applied to reach peak responsivity for all wavelengths (see Figure S6). This unique feature of our photodetectors allows us to access their full spectral range without changing biasing conditions as is required for some other detector systems^{22,23}. We note that the optimal voltage is dependent on the incident light power (see Figure S7).

In Figure 3d, we present the external quantum efficiency ($\text{EQE} = \mathfrak{R}hc/(\lambda e)$, where h is Planck's constant, c is speed of light in vacuum, and e is the electron charge) and specific detectivity ($D^* = \mathfrak{R}A^{1/2}/S_n$, where A is the detector area and S_n is the current noise spectral density averaged over the electrical bandwidth), obtained at -0.3 V as a function of laser energy up to 5.0 eV (see Methods). The frequency-dependent noise performance for this and another smaller device is shown in Figure S8. The EQE peaks at 30% in the near UV (3.1 eV), while the highest $D^* = 3.4 \times 10^9$ cm Hz^{1/2} W⁻¹ is observed in the MIR (0.52 eV), which is comparable to that of commercial IR detectors based on InAsSb or InSb²⁴. Furthermore, D^* remains on the order of 10^9 cm Hz^{1/2} W⁻¹ throughout the entire spectral range (except at the highest energy measured at 5.0 eV), enabling low light detection from MIR to all the way to DUV.

The response of I_{pc} to illumination on and off for two laser energies in the IR and visible are shown in Figure 3e. While the rise and fall times are all similar, the fastest response obtained is $\tau \sim 180$ ns, which corresponds to an electrical bandwidth of $0.35/\tau = 1.9$ MHz. We note that this speed is the fastest reported for photodetectors with comparable spectral range^{5-7,11-13}. For comparison, we have plotted the electrical bandwidth versus wavelength range for various commercially available and reported broadband detectors in Figure 3f. Our detectors have a clear performance advantage as they can achieve ultrafast response speed together with extremely broadband detection without the need for cryogenic cooling.

A key advantage of our device geometry is that the junction area size can be easily controlled to be smaller than the diffraction limit for IR radiation, enabling it for local spectroscopic measurements. First, we need to confirm that the active region is indeed localized within the overlap area between the three materials. We have thus performed spatially resolved photocurrent measurements by raster-scanning the focused laser. Figure 4 shows photocurrent imaging of two devices with different junction sizes ($16 \mu\text{m} \times 17 \mu\text{m}$ and $0.8 \mu\text{m} \times 0.8 \mu\text{m}$), each taken using two laser wavelengths in the visible (658 nm) and IR (2300 nm). The laser reflection images are shown in the panels on the left in grayscale. For the 658 nm laser, the spot size formed by the objective lens is $\sim 2 \mu\text{m}$ (see Figure S9a), which is larger than the junction area of the smaller device. Nonetheless, the strongest signal is clearly detected to originate from the overlap region of both, although there is a small decay outside the junction along the BP. The small features observed in the junction of the larger device correspond to unintended nonuniformities (wrinkles, bubbles, etc.) created during the fabrication process and can be recognized in the optical image as well.

For the 2300 nm laser, photocurrent images are taken using a reflective objective, which produces a series of circular fringes around the main focal spot (see Figure S9b). We thus attribute the bright features outside of the junction to imaging artifacts and not to the detectors themselves. We have further taken photocurrent spectra of both devices using the FTIR (see Figure S10). While the MIR response is slightly reduced in the device with smaller area, both produce a substantial photocurrent response down to 0.3 eV. These results

establish that our photodetector junction can still be responsive even when the size is scaled five times below its longest detectable wavelength of 4.1 μm .

We now finally demonstrate experimentally that our sub-wavelength photodetectors are sensitive enough to perform absorption spectroscopy on samples locally across the entire spectral range of detectivity. We have fabricated several small-area devices with junction sizes between $0.8 \mu\text{m} \times 0.8 \mu\text{m}$ and $3 \mu\text{m} \times 3 \mu\text{m}$ and illuminated them using a slightly focused tungsten lamp, which forms a relatively large $\sim 3 \text{ mm}$ diameter spot centered on the junction. We subsequently transfer various 2D materials on top for absorbance measurements. The inset of Figure 5a shows an optical image of a representative detector with 15-nm-thick Ta_2NiSe_5 above the active area and the upper panel shows photocurrent spectra in log scale taken before and after the transfer. The difference between the two curves is shaded in gray and yields the local absorbance spectrum shown in the lower panel. The α and β peaks at 1.5 eV and 2.2 eV, respectively, have been previously identified in bulk crystals²⁵. Importantly, we are also able to detect the peak in the MIR at $\sim 0.39 \text{ eV}$ (3180 nm)²⁶.

We have similarly obtained the absorbance spectrum of monolayer WSe_2 using this technique. An optical image of another detector with WSe_2 above is shown in the inset of Figure 5b. The color of the WSe_2 has been enhanced to highlight the thickness variation across the flake. Despite the sample nonuniformity, we can perform local spectroscopy only on the monolayer aligned on top of the junction. Even though the difference between the photocurrent spectra with and without WSe_2 is small (Figure 5b, upper panel), the absorbance spectrum can still be clearly extracted (Figure 5b, lower panel). The low overall sample absorbance (~ 0.06 maximum) is consistent with that of previous measurements using conventional techniques²⁷. The direct bandgap absorption onset edge is clearly seen at $\sim 1.5 \text{ eV}$, and the A and B excitons at 1.67 eV and 2.1 eV can be identified as well, all in agreement with the expected characteristics of monolayer WSe_2 ²⁸. Our photodetectors are thus able to resolve absorption features locally down to the single layer limit.

In summary, we have demonstrated a new photodetector concept based on 2D van der Waals heterostructures with high broadband detectivity from the MIR to DUV and fast response times that is operable at room temperature. The active device area can be scaled down to $0.6 \mu\text{m}^2$ and still sense IR radiation with wavelength longer than $4 \mu\text{m}$. Furthermore, the sensitivity is high enough to perform absorption spectroscopy on monolayer flakes under conventional widefield illumination. Such devices provide a new low-cost route towards local IR measurements beyond the diffraction limit without the need for high-cost and restrictive near-field techniques. By replacing BP with black arsenic phosphorus, the longest detectable wavelength may potentially be expanded to $8.2 \mu\text{m}$ ²⁹. Using nanofabrication, one may be able to decrease the size of the junction further, down to the nanoscale. Combined with large-scale films grown by chemical vapor deposition³⁰, one may even be able to develop dense pixel arrays using our heterostructure to perform hyperspectral imaging with super-resolution across over a decade in energy in the future.

Methods

Crystal synthesis. Black phosphorus (BP), hBN, WSe_2 and graphite single crystals were purchased from HQ graphene. 2H-MoTe_2 and Ta_2NiSe_5 single crystals were synthesized through self-flux and chemical vapor transport methods, respectively. For 2H-MoTe_2 , Mo (99.999%) and Te (99.999%) were introduced in a quartz ampoule in a ratio of 1:25 for growth in a Te flux. The tube was then heated up to $1100 \text{ }^\circ\text{C}$ and held for 24 h. Subsequently, the ampoule was cooled down to $525 \text{ }^\circ\text{C}$ at $2 \text{ }^\circ\text{C/h}$ and centrifuged. Plate-like 2H-MoTe_2 crystals with lateral dimensions up to millimeters were obtained and annealed at $425 \text{ }^\circ\text{C}$ for 2 days to remove residual Te. For Ta_2NiSe_5 , Ta, Ni, and Se powders (99.99%) were weighed in a ratio of 2:1:5 and mixed with 0.25 g of I_2 in a silicon quartz tube. Afterwards, the tube was sealed under high vacuum and put in a two-zone furnace. The hot side and cold side were kept at $950 \text{ }^\circ\text{C}$ and $850 \text{ }^\circ\text{C}$, respectively, for 7 days. The furnace was then closed and slowly cooled to room temperature.

Device fabrication. Gr/MoTe₂/BP heterostructures were fabricated using a layer-by-layer dry transfer method within a nitrogen-filled glove box (O₂ and H₂O levels below 0.1 ppm) to prevent oxidation³¹. All thin flakes were first exfoliated from bulk crystals onto a Si substrate with a 300-nm-thick oxide layer. A stamp made of polycarbonate (PC) on polydimethylsiloxane (PDMS) was used to pick up the top hBN, Gr, MoTe₂, and BP flakes from the Si substrate in sequence at 90 °C. The entire stack was then transferred onto a clean Si substrate with pre-patterned Au (45 nm)/Ti (5 nm) electrodes at 120 °C to delaminate the PC film and heterostructure from the PDMS. The residual PC was dissolved in chloroform at room temperature followed by rinsing in isopropyl alcohol. The thickness of the individual layers was subsequently determined using an atomic force microscope (AFM) (Bruker Dimension FastScan).

Broadband absorption and photocurrent spectroscopy. The absorption spectrum of BP and MoTe₂ flakes was measured using a Bruker IFS 66v/S FTIR spectrometer. A tungsten halogen source (OSRAM, 275W) was focused by a 36× reflective objective (Ealing, NA = 0.5) after the FTIR beamsplitter. The flakes were exfoliated onto transparent sapphire substrates. Transmitted light from the samples and substrate was collected by an in-built Si detector (Bruker D510) and liquid-nitrogen-cooled MCT detector (EG&G JUDSON J16D-M204-R05M-60) to obtain spectra at high and low energies, respectively. Photocurrent spectra of the detectors were measured using the same FTIR spectrometer. As prepared devices were wire-bonded onto 24-pin chip carriers and then mounted into an optical cryostat (Montana Instruments) with a CaF₂ window and kept under vacuum at room temperature. Different biases were applied to the device using a SourceMeter (Keithley 2450). The FTIR spectrometer was used with the broadband tungsten halogen source. Illumination from the tungsten halogen source was sent through the FTIR beamsplitter and then focused onto a ~ 3 mm spot centered on the device using a parabolic mirror (intensity ~ 2 W/cm²). The photocurrent signal was sent through a current pre-amplifier (Stanford Research Systems SR570), a voltage pre-amplifier (Stanford Research Systems SR560), and then fed back to the FTIR, which Fourier-transforms the signal to determine the spectral response. The relative spectral intensity of the source was also measured by three reference detectors: an in-built Si detector (Bruker D510), an MCT detector (EG & G JUDSON J16D-M204-R05M-60), and a biased, extended-range InGaAs detector (Thorlabs DET10D/M).

Laser-based photocurrent measurements. Laser diodes with wavelengths in visible ($\lambda = 405, 520,$ and 658 nm, Thorlabs) and IR ($\lambda = 820, 904, 1310, 1550$ nm, Thorlabs, and $\lambda = 2300$ nm, EblanaPhotonics) were focused onto the detectors using either a 15× reflective objective (Beck Optronic Solutions, NA=0.5) or regular 50× microscope objective (NA = 0.55). The intensity was adjusted by both changing the diode current and using neutral density filters. A Glan-Taylor polarizer and half-waveplate were used to control the linear polarization angle of laser. A scanning mirror galvo in the beam path was used to both position (for fixed-point measurements) and raster (for imaging) the focused laser spot across the device, while monitoring the reflected light using separate commercial photodetectors (Thorlabs PDA36A and DET10D/M for visible and IR, respectively). Bias voltages were applied to the detector using a Source Measure Unit (Keithley 2450 SMU) and the current was measured using a pre-amplifier (Stanford Research Systems SR570). For UV photoresponse ($\lambda = 250, 310,$ and 350 nm), a tunable pulsed laser (Light Conversion Pharos-SP, Yb:KGW) with pulse duration of 170 fs and repetition rate of 6 kHz was fixed on the detector, and average laser power and device current was used to determine responsivity. For rise/fall time measurements, the laser diode intensity was directly modulated using a square waveform from a function generator (Stanford Research Systems DS345). The current from device was sent through a current pre-amplifier (Femto DHPCA-100) in high-bandwidth mode to an oscilloscope (Siglent, SDS1104X-E).

Noise measurements. The device was enclosed in a dark environment for noise measurements. A home-made low-pass filter (circuit time constant ~ 20 ms) was used to cut the high-frequency noise from the voltage source (Keithley 2450 SMU). A lock-in amplifier (Stanford Research Systems SR830) was used to measure the device current noise as a function of ac frequency from 10 Hz to 100 kHz. The background noise was subtracted using the same measurement setup without the device in the current path, and the current noise power spectral density was obtained from fitting the frequency response to a power law.

Finite element numerical simulations. The dark current-voltage (I - V) characteristics were simulated in a one-dimensional model using the COMSOL Multiphysics Semiconductor Module. Taking the thickness values for each layer determined by the AFM, vertical structures of BP, MoTe₂, and Gr were constructed. The base simulation parameters of the individual layers, such as effective density of states of the conduction and valence bands at room temperature, doping concentration, bandgap energy, and electron affinity were taken from Ref ³² (see Supplementary Information, Table S1). The contacts at the end of the BP and Gr layers, are assumed to be ohmic. The spatially dependent energy band diagrams and carrier concentrations were extracted from the fittings to the I - V data.

Acknowledgements

We thank Michael Reimer and Jayakanth Ravichandran for a critical reading of our manuscript, and thank P. Sprenger and F. Sfigakis for assistance with experiments. A.W.T. acknowledges support from the US Army Research Office (W911NF-21-2-0136), Ontario Early Researcher Award (ER17-13-199), and the National Science and Engineering Research Council of Canada (NSERC) (RGPIN-2017-03815). This research was undertaken thanks in part to funding from the Canada First Research Excellence Fund. H.B.Y. and N.Y.K. acknowledge the support of Industry Canada and the Ontario Ministry of Research & Innovation through Early Researcher Awards (RE09-068). H.B.Y., C.S., and N.Y.K. acknowledge CMC Microsystems for COMSOL Multiphysics. Y.N.Z. and D.S. acknowledge NSERC and the Canada Research Chairs Program. T.T. was supported by NSERC grant “Optics of quantum materials.” D.A.R. acknowledges the support provided by the University of Wisconsin-Madison Office of the Vice Chancellor for Research and Graduate Education with funding from the Wisconsin Alumni Research Foundation. J.Y., X.L. and Y.P.S. thank the financial support from the National Nature Science Foundation of China under Contract Nos. 11674326, 11874357, the Joint Funds of the National Natural Science Foundation of China, the Chinese Academy of Sciences’ Large-Scale Scientific Facility under Contract Nos. U1832141, U1932217, and U2032215, the Key Research Program of Frontier Sciences, CAS (No. QYZDB-SSW-SLH015), the uses with Excellence and Scientific Research Grant of Hefei Science Center of CAS (No.2018HSC-UE011).

References

- [1] Tanner, D. B. *Optical Effects in Solids*. (Cambridge University Press, 2019). doi:10.1017/9781316672778.
- [2] Novotny, L. & Hecht, B. *Principles of Nano-Optics*. (Cambridge University Press, 2012). doi:10.1017/CBO9780511794193.
- [3] Huth, F. *et al.* Nano-FTIR Absorption Spectroscopy of Molecular Fingerprints at 20 nm Spatial Resolution. *Nano Lett.* **12**, 3973–3978 (2012).
- [4] Bechtel, H. A., Muller, E. A., Olmon, R. L., Martin, M. C. & Raschke, M. B. Ultrabroadband infrared nanospectroscopic imaging. *Proc. Natl. Acad. Sci. U.S.A.* **111**, 7191–7196 (2014).
- [5] Graf, A., Arndt, M., Sauer, M. & Gerlach, G. Review of micromachined thermopiles for infrared detection. *Meas. Sci. Technol.* **18**, R59–R75 (2007).
- [6] Long, M. *et al.* Palladium Diselenide Long-Wavelength Infrared Photodetector with High Sensitivity and Stability. *ACS Nano* **13**, 2511–2519 (2019).
- [7] Yang, M. *et al.* Three-Dimensional Topological Insulator Bi₂Te₃/Organic Thin Film Heterojunction Photodetector with Fast and Wideband Response from 450 to 3500 Nanometers. *ACS Nano* **13**, 755–763 (2019).
- [8] Konstantatos, G. *et al.* Hybrid graphene–quantum dot phototransistors with ultrahigh gain. *Nat. Nanotech.* **7**, 363–368 (2012).
- [9] Hayden, O., Agarwal, R. & Lieber, C. M. Nanoscale avalanche photodiodes for highly sensitive and spatially resolved photon detection. *Nat. Mater.* **5**, 352–356 (2006).
- [10] Yang, C., Barrelet, C. J., Capasso, F. & Lieber, C. M. Single p-Type/Intrinsic/n-Type Silicon Nanowires as Nanoscale Avalanche Photodetectors. *Nano Lett.* **6**, 2929–2934 (2006).

- [11] Koppens, F. H. L. *et al.* Photodetectors based on graphene, other two-dimensional materials and hybrid systems. *Nat. Nanotech.* **9**, 780–793 (2014).
- [12] García de Arquer, F. P., Armin, A., Meredith, P. & Sargent, E. H. Solution-processed semiconductors for next-generation photodetectors. *Nat. Rev. Mater.* **2**, 1–17 (2017).
- [13] Tan, C. L. & Mohseni, H. Emerging technologies for high performance infrared detectors. *Nanophotonics* **7**, 169–197 (2018).
- [14] Bullock, J. *et al.* Polarization-resolved black phosphorus/molybdenum disulfide mid-wave infrared photodiodes with high detectivity at room temperature. *Nat. Photon.* **12**, 601–607 (2018).
- [15] Yuan, S., Naveh, D., Watanabe, K., Taniguchi, T. & Xia, F. A wavelength-scale black phosphorus spectrometer. *Nat. Photon.* **15**, 601–607 (2021).
- [16] Kim, H. *et al.* Actively variable-spectrum optoelectronics with black phosphorus. *Nature* **596**, 232–237 (2021).
- [17] Zhang, G. *et al.* Infrared fingerprints of few-layer black phosphorus. *Nat. Commun.* **8**, 14071 (2017).
- [18] Ruppert, C., Aslan, O. B. & Heinz, T. F. Optical Properties and Band Gap of Single- and Few-Layer MoTe₂ Crystals. *Nano Lett.* **14**, 6231–6236 (2014).
- [19] Ling, X., Wang, H., Huang, S., Xia, F. & Dresselhaus, M. S. The renaissance of black phosphorus. *Proc. Natl. Acad. Sci. U.S.A.* **112**, 4523–4530 (2015).
- [20] Xia, F., Wang, H. & Jia, Y. Rediscovering black phosphorus as an anisotropic layered material for optoelectronics and electronics. *Nat. Commun.* **5**, 4458 (2014).
- [21] Ling, X. *et al.* Anisotropic Electron-Photon and Electron-Phonon Interactions in Black Phosphorus. *Nano Lett.* **16**, 2260–2267 (2016).
- [22] Tang, X., Ackerman, M. M., Chen, M. & Guyot-Sionnest, P. Dual-band infrared imaging using stacked colloidal quantum dot photodiodes. *Nat. Photon.* **13**, 277–282 (2019).
- [23] Huang, B. *et al.* High-Performance Perovskite Dual-Band Photodetectors for Potential Applications in Visible Light Communication. *ACS Appl. Mater. Interfaces* **12**, 48765–48772 (2020).
- [24] Infrared Detectors (Hamamatsu, 2021); https://www.hamamatsu.com/resources/pdf/ssd/infrared_kird0001e.pdf.
- [25] Larkin, T. I. *et al.* Giant exciton Fano resonance in quasi-one-dimensional Ta₂NiSe₅. *Phys. Rev. B* **95**, 195144 (2017).
- [26] Lu, Y. F. *et al.* Zero-gap semiconductor to excitonic insulator transition in Ta₂NiSe₅. *Nat. Commun.* **8**, 14408 (2017).
- [27] Ansari, N. & Ghorbani, F. Light absorption optimization in two-dimensional transition metal dichalcogenide van der Waals heterostructures. *J. Opt. Soc. Am. B* **35**, 1179–1185 (2018).
- [28] Li, Y. *et al.* Measurement of the optical dielectric function of monolayer transition-metal dichalcogenides: MoS₂, MoSe₂, WS₂, and WSe₂. *Phys. Rev. B* **90**, 205422 (2014).
- [29] Long, M. *et al.* Room temperature high-detectivity mid-infrared photodetectors based on black arsenic phosphorus. *Sci. Adv.* **3**, e1700589 (2017).
- [30] Cai, Z., Liu, B., Zou, X. & Cheng, H.-M. Chemical Vapor Deposition Growth and Applications of Two-Dimensional Materials and Their Heterostructures. *Chem. Rev.* **118**, 6091–6133 (2018).
- [31] Wang, L. *et al.* One-Dimensional Electrical Contact to a Two-Dimensional Material. *Science* **342**, 614–617 (2013).
- [32] Hu, S. *et al.* Gate-Switchable Photovoltaic Effect in BP/MoTe₂ van der Waals Heterojunctions for Self-Driven Logic Optoelectronics. *Adv. Opt. Mater.* **9**, 2001802 (2021).

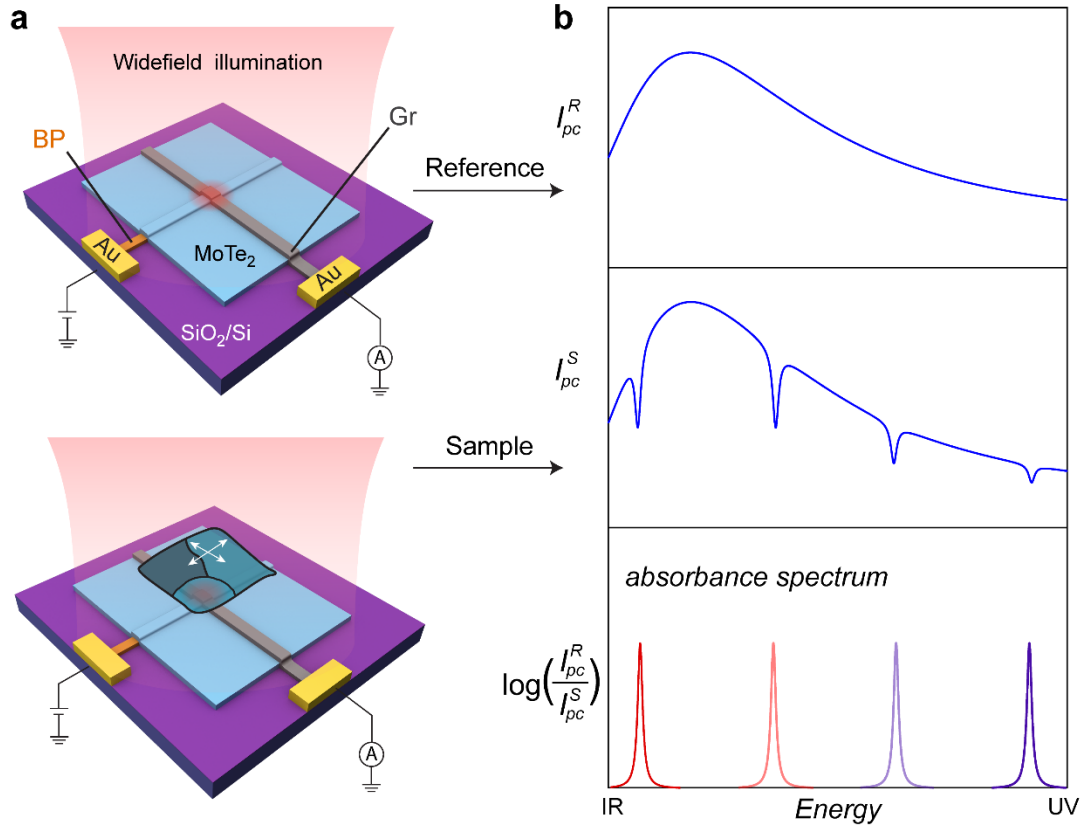


Figure 1. Miniature broadband photodetector based on 2D materials for local spectroscopy using widefield illumination. **a**, Geometry and measurement schematics of vertical BP/MoTe₂/Gr device before (top) and after (bottom) a nonuniform sample is aligned above the detector area (movement symbolized by white arrows). hBN covering layer is not shown. **b**, Corresponding photocurrent spectra with (I_{pc}^S) and without (I_{pc}^R) the sample. The local absorbance spectrum of the sample is obtained from logarithmic ratio of the two photocurrents, $\log(I_{pc}^R/I_{pc}^S)$.

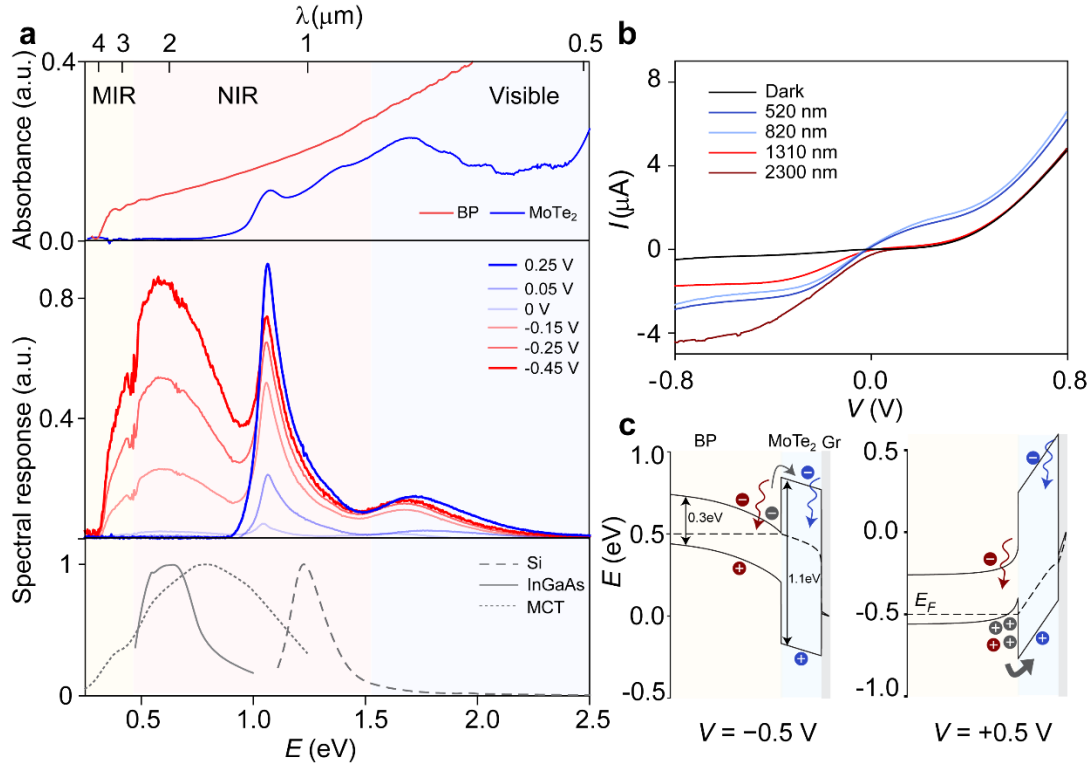


Figure 2. Spectral response and device modeling. **a**, (Top) Absorbance spectra of BP and MoTe₂. (Middle) Photocurrent spectra at six bias voltages taken under illumination by a broadband tungsten lamp. (Bottom) The light source spectra measured using three widely used commercial photodetectors based on Si, InGaAs, and MCT. **b**, I - V curves of device in dark and under illumination by focused lasers of several different wavelengths with 30 μW power and linear polarization fixed in direction generating maximum photocurrent. No substantial photocurrent is observed for IR light at positive V . **c**, Band structure diagrams of the heterostructure for $V = -0.5$ V (top) and $V = +0.5$ V (bottom) extracted from finite element simulations. Dark carriers in BP near the MoTe₂ interface are shown in gray. Photocarriers generated by IR and visible light are colored in red and blue, respectively. The large interfacial BP hole population under forward bias yields insignificant IR I_{pc} relative to I_{dark} .

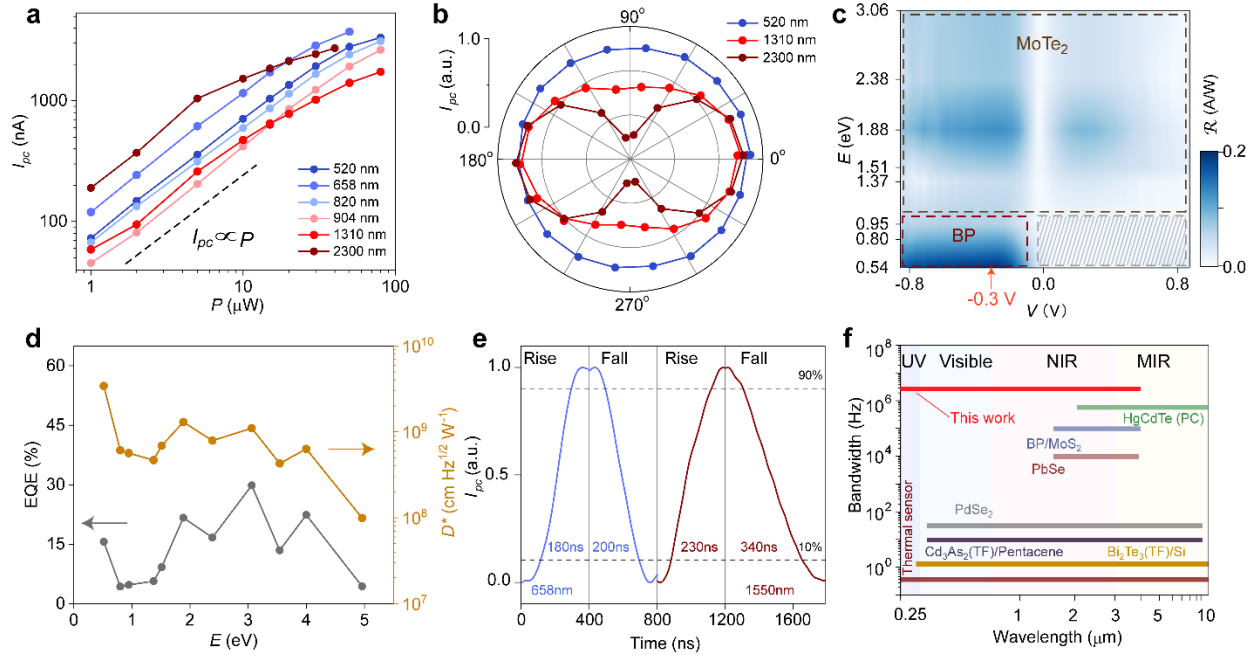


Figure 3. Characterization of photodetector performance metrics. Photocurrent I_{pc} as function of **a**, laser power and **b**, linear polarization angle for different laser wavelengths. **c**, 2D map of detector responsivity vs bias voltage and laser energy. The different photoresponse regions are boxed by dashed lines. Red arrow marks the voltage where quantum efficiency, detectivity, and rise/fall time are evaluated. The hashed area corresponds to where I_{pc} is insubstantial. **d**, External quantum efficiency (EQE) and specific detectivity (D^*) vs laser energy. **e**, 10-90% rise and fall times of I_{pc} measured with 658 nm and 1550 nm lasers on and off. **f**, Electrical bandwidth vs spectral response of Gr/MoTe₂/BP device compared with commercially available and reported broadband photodetectors.

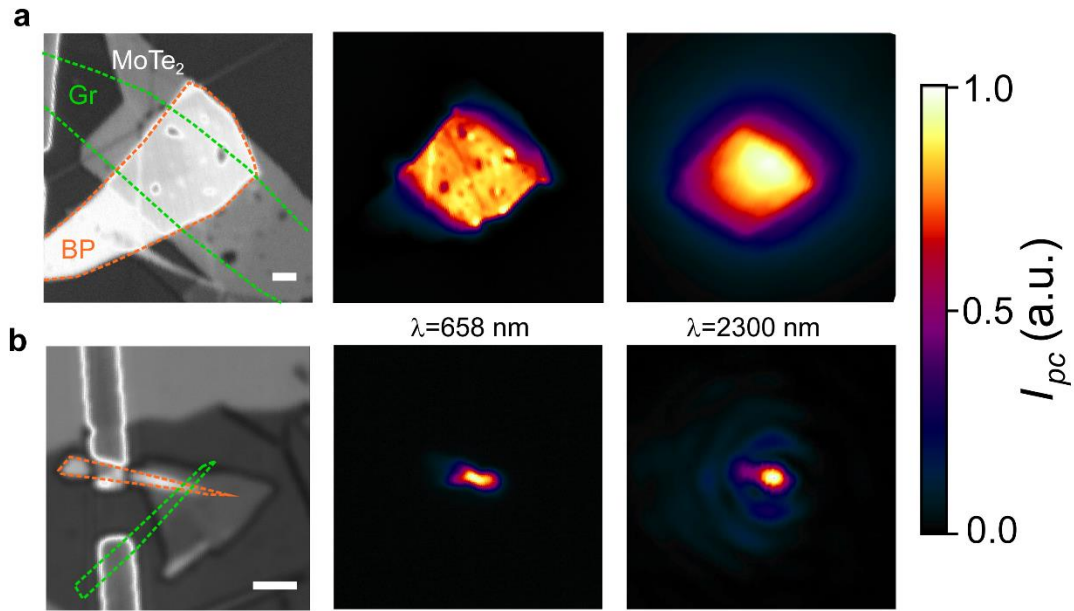


Figure 4. Spatially resolved photocurrent imaging of detectors. Reflection (left), 658 nm photocurrent (middle), and 2300 nm photocurrent (right) images of devices with **a**, $16\ \mu\text{m} \times 17\ \mu\text{m}$ and **b**, $0.8\ \mu\text{m} \times 0.8\ \mu\text{m}$ junction areas. Orange and green dashed lines outline the BP and Gr, respectively. Scale bars: $5\ \mu\text{m}$. Fringes in IR photocurrent are due to the use of a reflective objective.

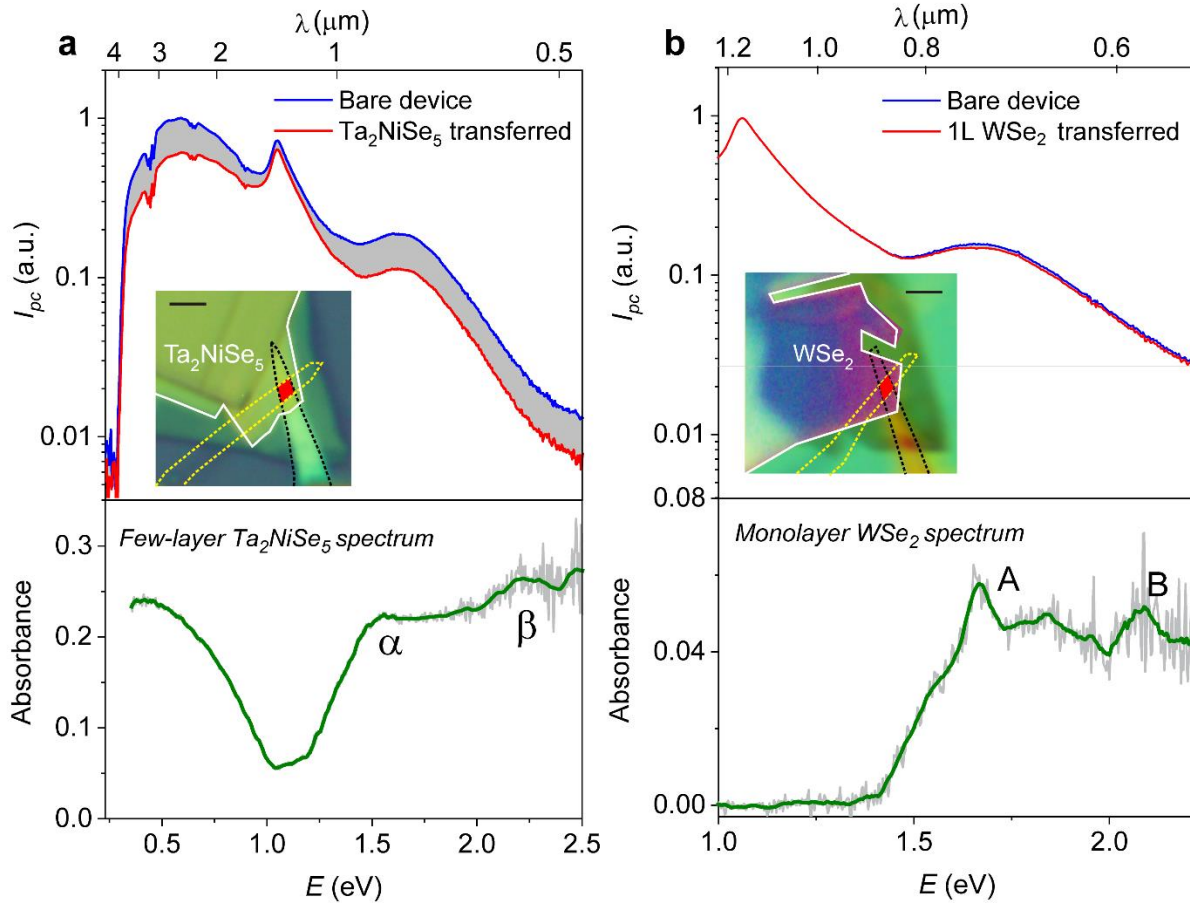


Figure 5. Demonstration of local spectroscopy capability on non-uniform 2D samples. **a**, Few-layer Ta_2NiSe_5 and **b**, Monolayer (1L) WSe_2 spectra. The inset images show ultrasmall photodetector devices ($0.8 \mu\text{m} \times 0.8 \mu\text{m}$) after non-uniform flakes are transferred on top. Black dashed lines, yellow dashed lines, and white solid lines outline the BP, Gr, and 2D sample, respectively. Scale bars: $2 \mu\text{m}$. A broadband tungsten source is focused by a parabolic mirror to a $\sim 3 \text{ mm}$ spot centered on the device junction marked by the red shaded area. The upper panels show photocurrent spectra of detectors with and without the 2D sample (difference shaded in gray). The bottom panels show absorbance spectra of thin Ta_2NiSe_5 and monolayer WSe_2 obtained from the procedure described in Figure 1. A background subtraction has been applied for WSe_2 . Raw (smoothed) absorbance data is shown in light gray (dark green). Higher noise at higher energy is due to lower intensity of the source. The photodetector can both resolve features down to a single atomic layer and yield broadband sensitivity down to 0.3 eV or $4.1 \mu\text{m}$, larger than the width of the junction.